



Investigation and numerical modeling of the overloading-induced catastrophic rockslide avalanche in Baige, Tibet, China

Wenpei Wang¹ · Yueping Yin¹ · Sainan Zhu¹ · Lichao Wang¹ · Nan Zhang¹ · Ruixin Zhao²

Received: 21 July 2019 / Accepted: 2 November 2019 / Published online: 28 November 2019
© Springer-Verlag GmbH Germany, part of Springer Nature 2019

Abstract

After the first high-position landslide occurred in Baige Village, a second slide originated from the crown of the first landslide on November 3. The approximately 1.6 million m³ second slide moved rapidly and applied an impact load on the upper part of the residual mass of the first landslide, resulting in a 6.6 million m³ entrainment volume. The sliding mass rushed into the Jinsha River and blocked the channel again, causing catastrophic flooding which destroyed numerous roadbeds, bridges, and a large number of residential houses in Sichuan and Yunnan provinces. Based on field investigations and simulation results by dynamic discrete element method (DEM), after the first landslide, the blocks formed by the trailing edge of the landslide became unstable and slid, continuously and dynamically loading and accumulating on the upper part of the first debris deposit, which rested in the grooved terrain of the slope, leading to the instability of the residual slope's rock–soil mass and the initiation of a debris avalanche. With a peak velocity of 62 m/s, the debris avalanche slid rapidly to the location of the first slide deposit. Due to the topographic effect, it was transformed into a diffused debris avalanche, which scattered and accumulated, exhibiting the typical characteristics of a rapid long-runout landslide. Then, the calculated velocity value by DEM was also compared with those using other dynamic modeling approaches (e.g., sled model and rheological model). The DEM was proven producing a reasonable velocity variation pattern, and thus, it is suitable for the simulation of the entire movement process of high-position rockslides similar to the second Baige landslide.

Keywords Rockslide · Overloading effect · Dynamic erosion effect · Discrete element method · Unstable blocks

Introduction

Recently, successive landslides and repeated damming occurred along the Jinsha River over a very short period of time. At 10:06 PM on October 10, 2018, the first high-position landslide occurred in Baige Village, Jiangda County, Tibet, 515 km from Chengdu, Sichuan, which is also on the upper reaches of the Jinsha River (Fig. 1). The landslide had a total volume of approximately 35 million m³, an elevation difference of 834 m, and a sliding direction of 82°. After sliding, it induced a 160-m-high surge wave, which crashed into the left bank and dammed the river. Two days later, at 17:15 on

October 12, water naturally overtopped and overflowed the barrier lake. At 00:45 on October 13, the upstream inflow of the barrier dam was balanced by the outflow of the breached dam, reaching a total storage of 290 million m³. At approximately 5:00, the flow rate at the breach reached a peak of 10,000 m³/s; and at 12:00, the flow rate at the breach was attenuated to approximately 2000 m³/s. Fortunately, this landslide did not pose a greater hidden danger. However, at 17:15 on November 3, a second slide originated from the crown of the first landslide. The second landslide, which had a slide volume of about 1.6 million m³, slid rapidly and applied an impact load on the upper part of the residual mass of the first landslide, leading to an entrainment volume of approximately 6.6 million m³. The sliding mass rushed into the Jinsha River and blocked its channel again. At 15:00 on November 6, the water storage was approximately 212 million m³. By 11:00 on November 11, excavation of an artificial drainage tank was completed. At 13:40 on November 13, the water storage was 578 million m³. At 18:00, the flow rate at the breach in the barrier dam reached a peak of 31,000 m³/s. On the morning of

✉ Yueping Yin
yyueping0712@163.com

¹ China Institute of Geo-Environment Monitoring, China Geological Survey, Beijing, China

² Chang'an University, Xi'an, China

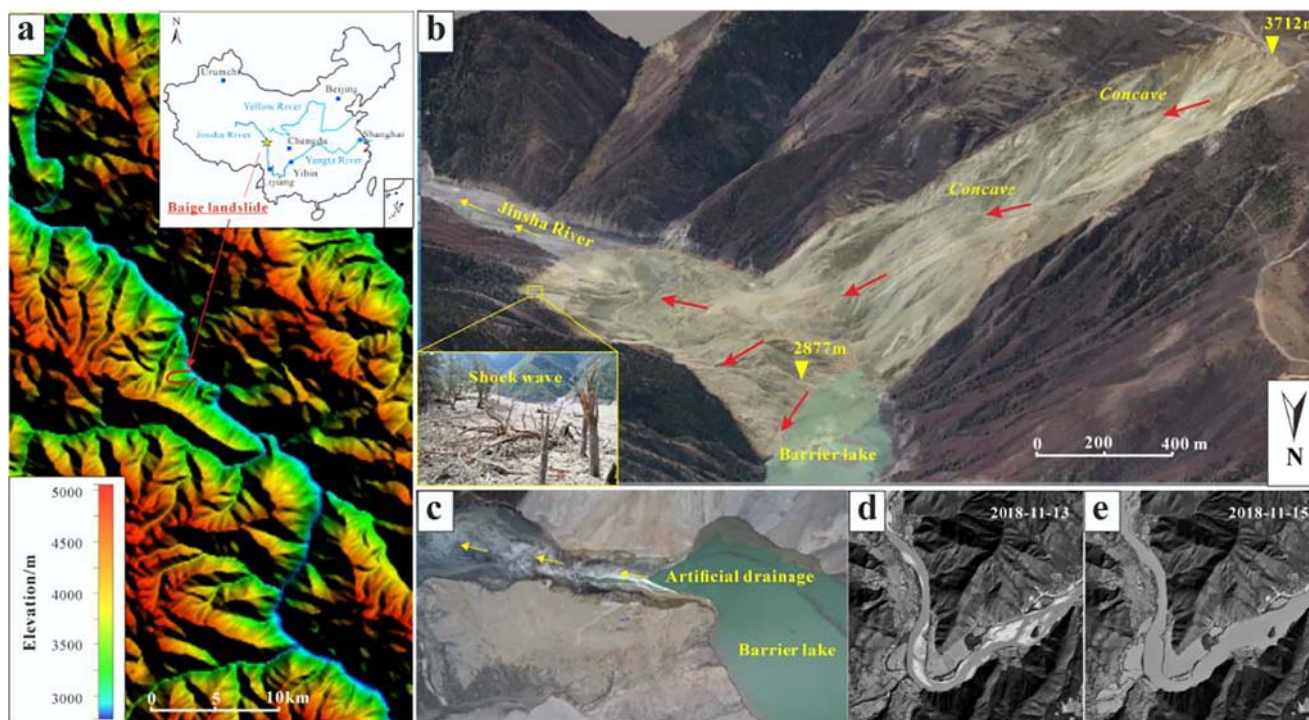


Fig. 1 Location of the two landslides in Baige, Tibet, southwestern China. (a) The two Baige landslides along the Jinsha River; (b) 3D image of the landslide taken by an unmanned aerial vehicle (UAV) on November 9, 2018; (c) a spillway was excavated to reduce the rising water level caused by the new landslide dam, which was formed on

November 3, 2018; (d) a remote image of Shigu Town, Lijiang, on November 13, 2018, i.e., before the upstream flood; (e) a remote image of Shigu Town, Lijiang, on November 15, 2018, i.e., after the upstream flood

November 14, the breach discharge was equal to the upstream inflow, and the water flow returned to normal (Fig. 2). However, the overflowing flood peak of the Baige Barrier Lake on the Jinsha River entered the Sichuan and Yunnan provinces. Numerous roadbeds and bridges were destroyed by floods, and a large number of residential houses on the banks of the lower reaches of the river were flooded, causing significant economic loss (Fan et al. 2019; Ouyang et al. 2019; Deng et al. 2019; Xu et al. 2018; Wang et al. 2019a).

The occurrence of a catastrophic high-position landslide is not just a coincidence in time and space, especially in seismically affected mountainous regions (Fan et al. 2018). Chain-reaction style geological disasters often occur in seismically affected areas and often, sudden slides from the ridge crest or high positions on steep slopes, impact and entrain a large volume of surface material, producing a high-speed debris avalanche, which is then transformed into a debris flow that will accumulate and even block the frontal river valley (Yin et al. 2016). In particular, when the landslide rapidly disintegrates and is transformed into a debris avalanche along the direction of movement, due to its high impact energy and high mobility, it has an entrainment effect on the basement along the movement path, resulting in the amplification of the volume of the debris avalanche and the rapid long-runout of the movement. On July 13, 2013, a catastrophic high-position

landslide–debris flow occurred in Sanxi Village, Dujiangyan City, Sichuan Province, with an initial landslide volume of about $147 \times 10^4 \text{ m}^3$. It disintegrated upon impact and was transformed into a debris avalanche. The debris flow formed along the gully, causing 166 deaths. The landslide had an elevation difference of 420 m between its leading and trailing edges, a movement distance of about 1.2 km, a final deposit volume of $191.5 \times 10^4 \text{ m}^3$, and an entrainment volume of $44.5 \times 10^4 \text{ m}^3$. On June 24, 2017, a catastrophic high-position, long-runout landslide–debris avalanche occurred in Xinmo, Maoxian, Sichuan Province. The initial landslide volume was only $390.6 \times 10^4 \text{ m}^3$, but the sliding distance exceeded 2.8 km due to an elevation difference of 1200 m between the leading and trailing edges of the landslide. The strong entrainment of the basement during the movement increased the accumulation volume of the debris avalanche, which had a final volume of $1637.6 \times 10^4 \text{ m}^3$ (more than 4 times that of the original volume). This landslide destroyed Xinmo Village and killed 83 people.

At present, the most representative dynamic erosion models of long run-out landslides are self-undrained loading models (also called liquefied models), rheological models, grain flow models, sled models, and discrete element models (Hung et al. 1995; Hung and McDougall 2009; Sassa et al. 2010, 2014; Xing et al. 2014; Zhang and McSaveney 2017).

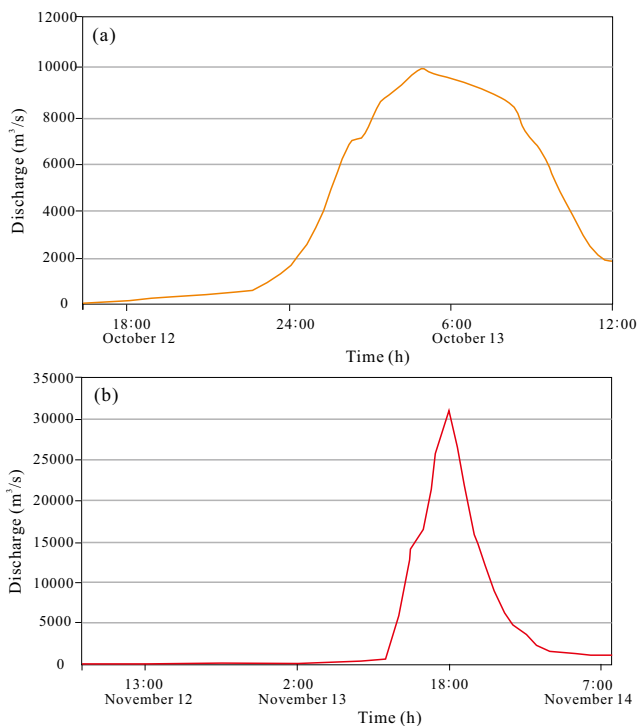


Fig. 2 Variations in discharge over time (data is from the Bureau of Hydrology, Changjiang Water Resources Commission). (a) The flood hydrograph curve of the first landslide dam break in October; (b) the flood hydrograph curve of the second landslide dam break in November

The first type of model takes into account the excess pore water pressure and the numerous rheological relationships due to loading, whereas the second type takes into account the volume increase due to shovel scraping. The grain flow model uses mechanical fluidization and the fragmentation pressure to explain the fragmenting granular flow or similar flow of rock fragments (Davies and McSaveney 1999; McSaveney and Davies 2007). More recently, 3D discrete-element packages, i.e., the Engineering Discrete Element Method (EDEM) and the Particle Flow Code (PFC), are increasingly being used to simulate the granular nature of the flow of landslide material, including the collisional and frictional interactions between all of the particles and between the particles and the basal surfaces (Feng et al. 2017; Cagnoli and Piersanti 2017; Chen et al. 1998). Their parallel processing abilities make it easier to simulate, visualize, and analyze extremely large particle systems. In particular, based on rolling motion of particles in PFC software, a new progressive scouring entrainment model was put forward, which can be used to estimate the entrainment rate in granular flow (Kang and Chan 2018).

The actual dynamic erosion process of a high-position, long-runout landslide–debris avalanche is quite complex. However, previous studies of mechanical modeling have mainly been based on experimental simulations that assume excess pore water pressure and shear stress transfer. The

mechanism for mechanical transfer between the landslide–debris avalanche and the basement material is usually simplified as the surface shear force, which is unable to fully consider the dynamic erosion effect and the accumulated loading effects caused by the impact (Yin et al. 2017).

In this paper, based on field investigation and numerical analysis, we use the second Baige rockslide avalanche along the Jinsha River as an example to analyze the overloading and entrainment processes and the related dynamic characteristics of long runout landslides.

Environmental geologic setting

In terms of geomorphology, the Baige landslide is located on the right bank of the valley in the Hengduan Mountains and the Jinsha River Basin in eastern Tibet. It is located along the Jinsha River suture zone. Due to the influence of multi-phase tectonic movements, the mylonization and alteration of the rocks in this area are severe ($31^{\circ} 04' 54.91$ N, $98^{\circ} 41' 52.15$ E; Fig. 1). The fold and fault structures in the strata are well developed. The fold structure in the area is characterized by multiphase transformation and complex superimposed folds. The traces of the main fault structure in the study area include the near NS-trending Jiangda-Bolo-Jinshajiang fault zone and the NW-trending fault. There are one or more weak structural planes in the rock mass near the fault zone. These planes form a good channel for weathering agents to erode the rock, and thus, weathering of the rock in these areas has been accelerated, providing favorable conditions for the formation of geological disasters such as the Baige landslide.

The lithology of the outcropping strata in the Baige landslide area is mainly composed of the Gangtuo Formation (PT_{1g}), the gneiss formation, and the Hualixi serpentine belt (φ_{w4}). The gneiss formation has a schistosity of $180^{\circ}\text{--}220^{\circ}\angle 36^{\circ}\text{--}42^{\circ}$, and developed structural planes of $60^{\circ}\text{--}80^{\circ}\angle 75^{\circ}\text{--}85^{\circ}$ and $100^{\circ}\text{--}115^{\circ}\angle 80^{\circ}$. The serpentinite belt occurs in the upper part of the slope and exhibits good crystallization at the top of the slope, and its middle and lower parts have been pulverized. The chloritization reveals multiple episodes of multi-phase deformation and metamorphism. The silty rocks and chlorite exhibit multiple episodes of deformation and metamorphism. The fine-grained and clayey soils of the slope were continuously precipitated by groundwater and are the main lithology of the slide zone's soil. During normal and heavy rain events, rainwater flowed through the cracks, increasing the unit weight of the slope's rock and soil and infiltrating and softening the rock and soil mass of the sliding surface. As a result, the shear strength

of the rock and soil mass decreased, making the slope prone to instability.

This area has an earthquake intensity of VII. In recent years, there many earthquakes have occurred near the landslide area. In particular on August 12, 2013, a magnitude 6.1 earthquake occurred in the nearby city of Changdu (30.0° north latitude and 98.0° east longitude), which further loosened and degraded the rock mass.

According to the rainfall data provided by the nearest weather station in Ronggai Township, which is 15 km away from the landslide location, the average and maximum annual precipitation in the landslide area are 650 mm and 1067.7 mm, respectively. After the beginning of the flood season in 2018, the rainfall was greater than that during the same period in previous years. Between August 1, 2018, and the onset of the first landslide, the cumulative rainfall at the station was 214 mm (Fig. 3), accounting for one-third of the annual average precipitation. The abundant rainfall exacerbated the occurrence of landslides. However, no significant precipitation occurred during the 7 days before the second landslide, suggesting the lack of an obvious correlation between rainfall and the landslide events.

According to the hydrogeological survey data, the groundwater in the landslide area mainly occurs as loose rock pore water and bedrock fissure water. A series of gullies existed on the right side (south side) of the landslide area, accommodating surface and subsurface flow, which softened the slide zone's soil (mainly silty clay).

In addition, bedrock fissure water seeped from the surface of the landslide's wall, playing an important role in softening the soil mass. However, the second landslide was composed of dry gravelly silty soil, which was unaffected by groundwater.

Based on multi-period remote sensing image analysis and an actual ground survey of the landslide, the first Baige landslide had an area of approximately $88 \times 10^4 \text{ m}^2$, a longitudinal length of about 1600 m, a maximum width of about 700 m, an average width of about 550 m, an elevation difference of 834 m between the leading and trailing edges, a slope of about 35°–65° at the leading edge and in the middle-to-rear sections of the landslide, and a slope of 75° locally at the back wall of the landslide. The main body of the second Baige landslide included the trailing edge and both sides of the first landslide, producing an irregular shape (Figs. 4 and 5). The second landslide was characterized by rapid sliding of the high-position residual block in the direction of about 85°. The second landslide applied an impact load to the rock and soil layer of the slope formed by the first landslide deposit, which caused the sliding mass to disintegrate and fragment, transforming into a rapid long-runout debris avalanche, which backfilled the flood relief channel of the first landslide. Based on its dynamic characteristics, the second Baige landslide can be divided into the slide source area, the sliding entrainment area (impact loading area), and the accumulation area of the landslide–debris avalanche.

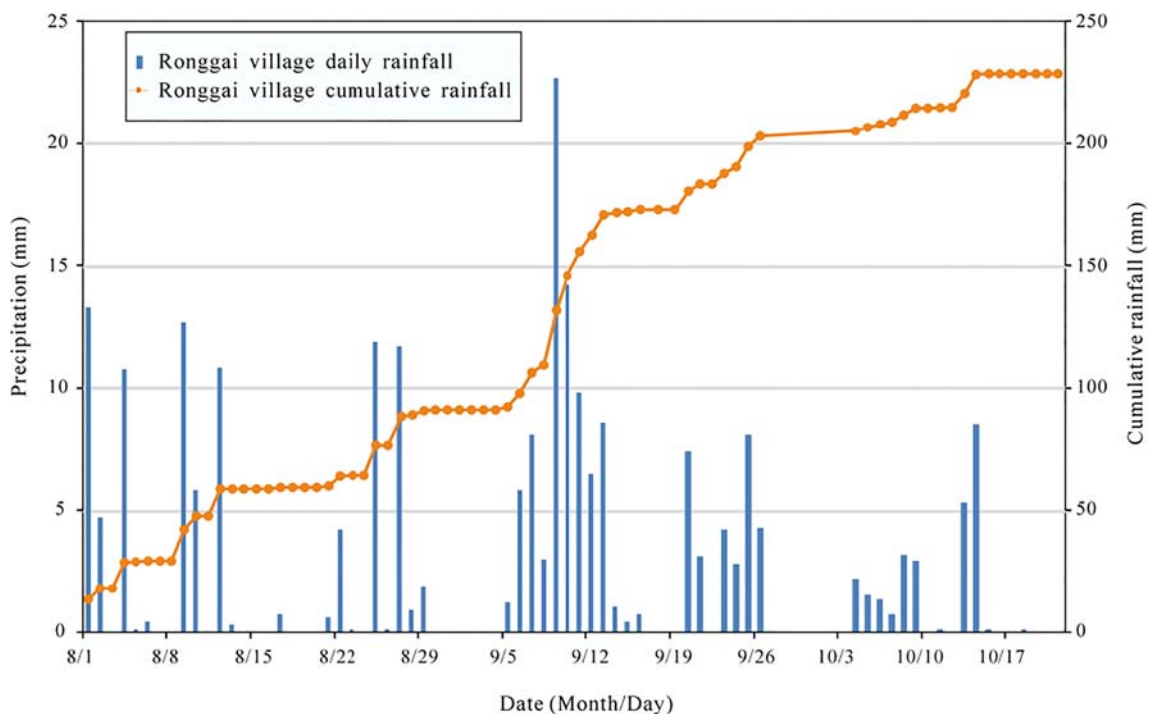


Fig. 3 Rainfall records for August 1 to August 10 of 2018

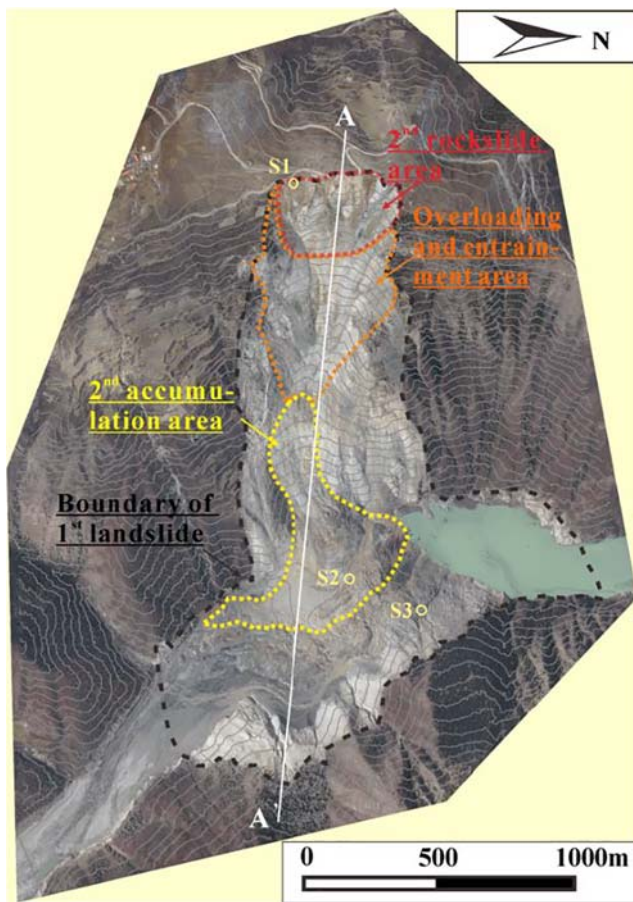


Fig. 4 Zone map of the second rockslide–debris flow in Baige. The yellow circle represents the window for analyzing the grain-size distribution

Post-failure characteristics of the second rockslide avalanche

Source area

The source area of the second landslide is located at an elevation of 3474 to 3718 m with a height difference of 244 m. The slope is steep and has an inclination angle of 50° (Figs. 5b, c and 6a), and it mainly formed as an unstable block at the trailing edge of the first landslide. The right side of the crack at the trailing edge of the block extends along the country road with a strike of 0° N to 10° W. The left side of the crack is deflected to approximately $N40^\circ$ E, intersects with the front free surface, and already exhibits coalescence prior to reaching the landslide. The unstable block is a triangular block protruding forward with a sliding zone on both sides. The total volume of the landslide is approximately 1.6 million m^3 . The parent rock stratum is the Hualixi serpentine belt, and overall, it is very fragmented and severely weathered. The structural surface has been completely weathered and/or filled with calcite. The rock mass of the back wall of the landslide is a greenish white serpentine wall that exhibits chloritization.

Since the rock mass was fragmented, small-scale collapses constantly occurred after the occurrence of the landslide.

Overloading and entrainment area

The overloading and entrainment area is located at an elevation of 3041 to 3474 m. The dip length of the debris avalanche area is about 960 m. Along the V-shaped chute formed by the first landslide, the inclination of the slope is significantly smaller and has an angle of 27° . According to the remote sensing image analysis and a field survey conducted before the second landslide occurred (Figs. 5b, c and 6b), the original slope deposit was a debris deposit formed by the first landslide. The grooved terrain of this slope provided a good deposition site. The deposit material was composed of slightly wet, gray, grayish white, and purple gravelly soil. The angular gravel in the soil is mainly 5 to 50 cm in size; the gravel content of the soil is about 30 to 40%. The deposit has a length of about 856 m, a maximum thickness of 40 m, an average thickness of 15 m, a width of 500 m, and a volume of about 6.6 million m^3 . After the landslide in the source area became unstable, it quickly transformed into a debris fluid. Then, it dynamically impacted and loaded the deposit material along its path, forming a significant sliding area after loading and rapidly increasing both the volume and velocity of the debris avalanche.

Accumulation area

According to the remote sensing image analysis and the field survey, the slope of the local terrain in the barrier accumulation area increased from 27° to 39° , which further accelerated the velocity of the debris avalanche and increased the impact force. In the early stage, the debris avalanche, in the form of diffusion flow, overlapped the barrier accumulation area formed by the first landslide and blocked the natural discharge channel. As a result, the average height of the dam increased by 50 m, the total volume of the deposit was about 30.2 million m^3 , and the width of the later-stage artificial flood relief channel was about 100 m. The ratio of soil to rock in the accumulation area was about 8:2 (Figs. 5b, c and 6b).

The grain-size distribution of the surface of the deposit (Fig. 7) was estimated at 4 sample sites (Figs. 4 and 5). The sample sites were located in the debris avalanche and debris flow areas. Each of the grain-size distributions was divided into four grain-size groups: > 100 cm, 50–100 cm, 10–50 cm, and < 10 cm. The gravels were generally fine-grained. For all of the sampling sites, the proportion of gravels less than 50 cm in size was more than 70%, while that of sites S2 and S3 on the surface of the barrier dam was more than 90%.

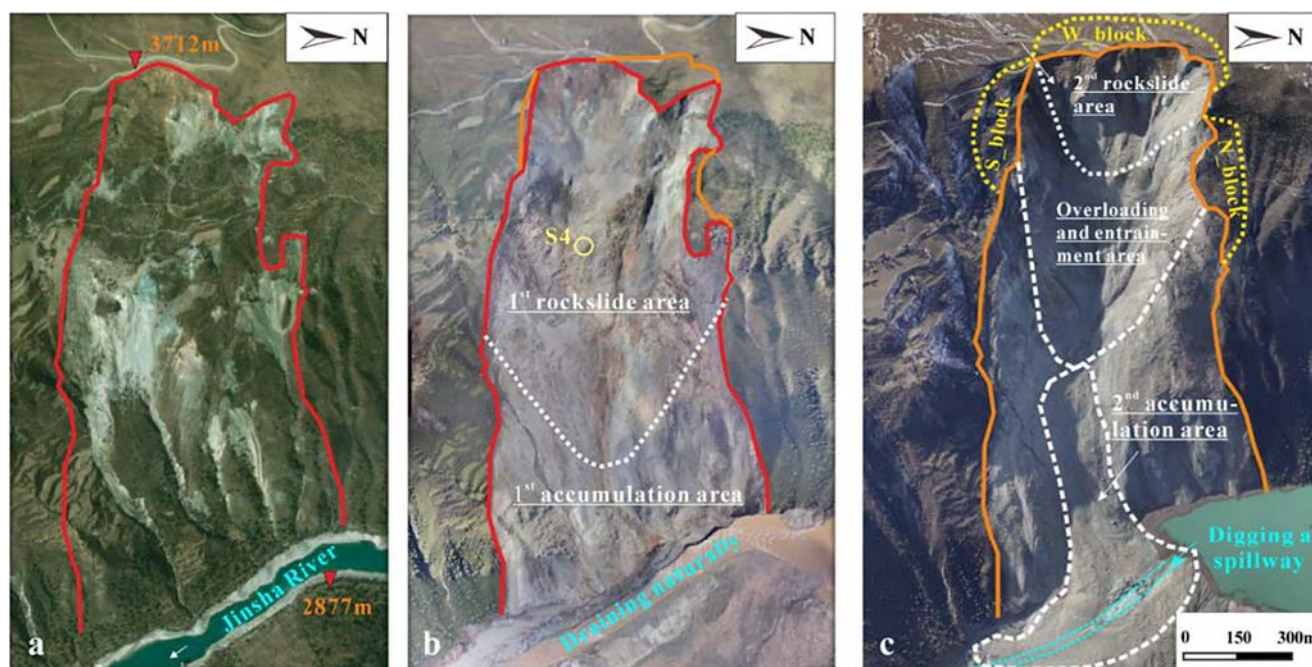


Fig. 5 Images of the development stages of the two landslides in Baige. (a) PlanetScope image taken on August 29, 2018; (b) full-view image taken by a UAV on October 16, 2018. The yellow circle represents the window for analyzing the grain-size distribution; (c) 3D image taken by a

UAV on November 9, 2018. The yellow dots represent the southern, western, and northern unstable boundary blocks, i.e., the S_block, W_block, and N_block, respectively

Unstable blocks

According to the remote sensing image analysis and the field survey, after both landslides occurred, the landslide was continuously strengthened due to the unloading effect on the free surface, and it continued to undergo significant deformation. Multiple large, deep cracks developed on the trailing edge and on both sides of the landslide, and a large number of loose unstable blocks were still present. Based on their positions, the distribution of the cracks at the trailing edge of the landslide, and the characteristics of the slope structure and deformation, there are three unstable blocks: the western, northern, and southern blocks (Fig. 5c). The volume of each block was calculated using the 3D Analyst tool. The western block (W_block) is located at the top of the back wall of the landslide, contains transverse cracks, and has a volume is about $1.8 \times 10^6 \text{ m}^3$. The southern block (S_block) is located on the right side of the trailing edge of the landslide, and has a volume of about $1.15 \times 10^6 \text{ m}^3$. There are coalescing cracks at the trailing edge, which are more than 100 m in length and 0.3 m in width. The northern block (N_block) is located on the left side of the landslide, and has a volume of about $1 \times 10^6 \text{ m}^3$ (see Table 1 for details).

The W_block was mainly formed by traction unloading of the two landslides. Its deformation is mainly characterized by the development of a large number of transverse tensile cracks, dense reticular cracks in the gravelly soil

layer of the leading-edge of the block, and small-scale slips (Fig. 8). The crack is approximately arc shaped. It has a length of about 120 to 130 m, a width of up to 40 cm, a fault distance of up to 50 cm at the bottom, and a visible depth of up to 60 cm. The crack has good continuity and is located a maximum distance of 40 m from the trailing edge of the landslide. The W_block mainly consists of Quaternary gravelly moraine soil (the surface layer is meadow soil), gneiss, and phyllite.

The S_block was mainly formed by the traction unloading and entrainment of the two landslides. Its deformation is mainly characterized by the development of a large number of transverse and longitudinal tensile cracks on the slope, the development of coalescing shear cracks on the right side, and small-scale slips at the leading edge (Figs. 8 and 9). The trailing edge of the block is bounded by a steep fault scarp, the leading edge is bounded by a steep scarp, which creates a seepage point, and the right side is bounded by the last level of a steep shearing scarp. The block is mainly composed of Quaternary gravelly broken block soil, gneiss, and phyllite.

The N_block was directly formed by traction unloading of the landslide and has a tongue-shaped plane. Its deformation is mainly characterized by the development of a large number of transverse, longitudinal, and bulging cracks, the development of coalescing shear cracks on the left side, and small-scale slips at the leading edge. The shear outlet is significant at the leading edge and is

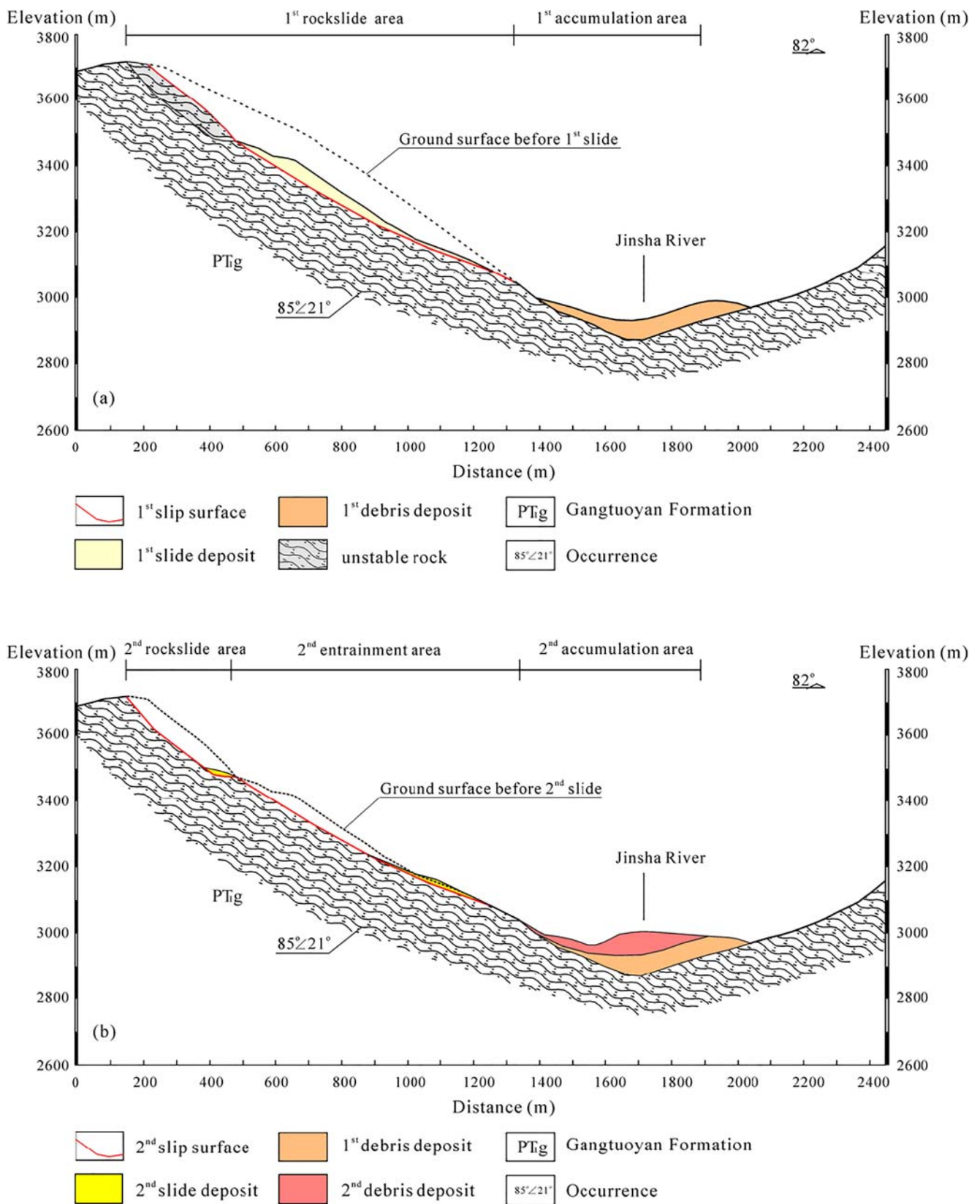
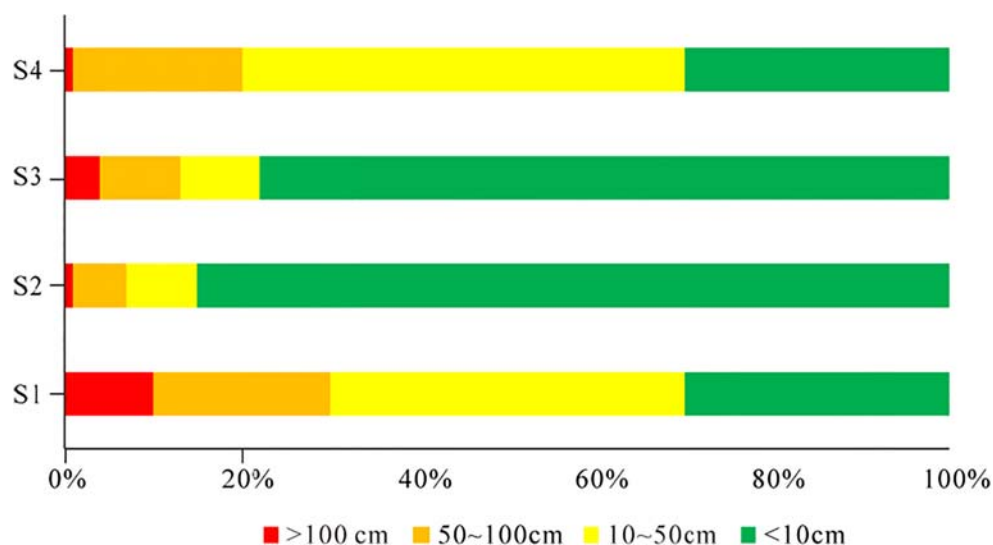


Fig. 6 Engineering geological section along profile line A-A' before and after the second landslide. (a) before sliding; (b) after sliding

currently in a state of uniform deformation (Fig. 9). The trailing edge is bounded by the last level of coalescing

cracks, the leading edge is bounded by a steep scarp, which produces the slip, and the left side is bounded by the last

Fig. 7 Grain-size distribution at 4 observation points on the surface of the deposit



level of shear cracks, which extend downward. From top to bottom, the block is mainly composed of Quaternary gravely broken block soil and gneiss.

According to the monitoring data from the displacement meters and crack meters deployed on the surface of the three unstable blocks (Wang et al. 2019a), the W_block is intensely deformed and has a continuously increasing deformation rate, resulting in the possibility of small-scale collapse and slide. The N_block is in the rapid deformation stage characterized by small to medium-sized landslides. The S_block has a relatively stable deformation rate, and no significant change has been observed in its cracks.

Runout simulation analysis

EDEM® is a CAE (Computer Aided Engineering) software that simulates particle movement and their interaction based on DEM method (Cundall and Strack 1979; EDEM 2018). It calculates the relative displacement and unbalanced force between particles through Newton's second law of motion. The physical information and force of each particle can be recorded and output, and the data will be updated through iterations per time step. It has the ability to simulate a rock avalanche,

debris flow and collapse, and can estimate the dynamic behavior of a landslide.

Contact model

In the EDEM, the mechanical properties of the contact and the separation of the particles are simulated using the contact constitutive model. The contact constitutive models of the EDEM are the Hertz-Mindlin (no slip), the Hertz-Mindlin with Bonding, Linear Cohesion, Hysteretic Spring, etc. The Hertz-Mindlin (no slip) model (Fig. 10) was selected as the contact model for the simulation due to its accurate and efficient force calculations. It consists of the normal force, the tangential force components, and the resistance. The normal and the tangential force components are based on the Hertzian contact theory and the Mindlin-Deresiewicz theory. They both have damping components for which the damping coefficient is related to the coefficient of restitution (Tsuji et al. 1992). The resistance is limited by the Coulomb static friction and rolling friction coefficients. The main micromechanical parameters used for the subsequent dynamic analysis, are presented in Table 2. Based on the field investigations, we often use “virtual experiment” calibration to determine micromechanical

Table 1 Volume of the unstable boundary blocks

Group	Area ($\times 10^3 \text{ m}^2$)	Thickness ($\times 10^3 \text{ m}$)	Volume ($\times 10^3 \text{ m}^3$)	Description
W_block	88.9	20	1778	The deformation was large and the deformation rate was continuously increasing.
S_block	57.3	20	1146	The deformation rate was relatively stable.
N_block	68.3	15	1024.5	In a state of rapid deformation.



Fig. 8 Main characteristics of the W_block. (a) Location of the tension cracks after the second landslide; (b) local sliding after the first landslide; (c) local sliding after the second landslide; (d) crack opening width of up to 30–50 cm; (e) tension cracks developing; (f) imbricated cracks

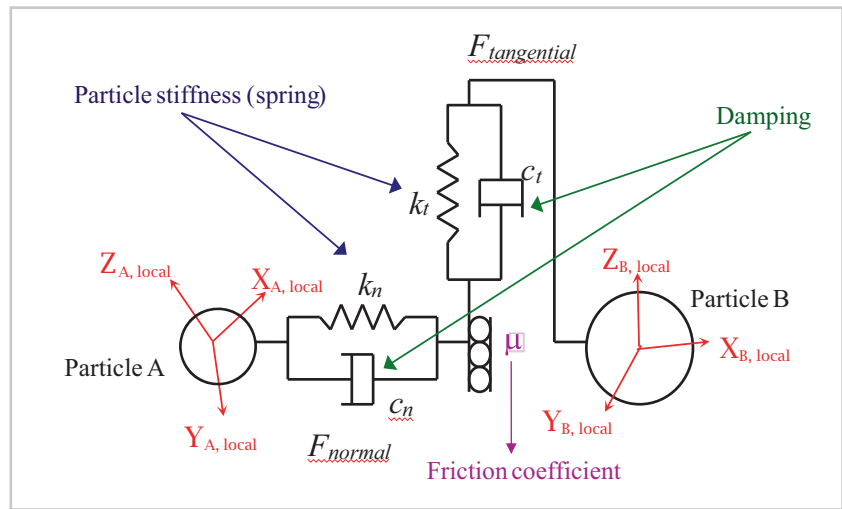
parameters in discrete element method. The values of the contact model and the parameters between the particles are

consistent with those between the particles and the path topography. The related equations are



Fig. 9 Main characteristics of the N_block and S_block. (a) The boundary characteristics after the second landslide; (b) extremely fragmented gneiss; (c) transverse tension cracks; (d) local sliding; (e) weathered serpentinite; (f) local sliding; (g) deposit composed of loose gravel and soil

Fig. 10 Schematic diagram of the Hertz-Mindlin (no slip) contact model for the DEM



$$\begin{cases}
 F_n = \frac{4}{3} E \sqrt{R'} \delta_n^3 \\
 F_t = -8 \delta_t G^t \sqrt{R' \delta_n} \\
 F_n^d = -2 \sqrt{\frac{5}{6}} \frac{\ln e}{\sqrt{\ln^2 e + \pi^2}} \sqrt{S_n m' v_n^{rel}} \\
 F_t^d = -2 \sqrt{\frac{5}{6}} \frac{\ln e}{\sqrt{\ln^2 e + \pi^2}} \sqrt{S_t m' v_t^{rel}} \\
 T_r = -u_r F_n R_i \omega_i \\
 T_s = -u_s F_n
 \end{cases} \quad (1)$$

where the normal force F_n is a function of the normal overlap δ_n . E and R' are the equivalent Young's Modulus and the equivalent radius derived from the Young's Modulus, the Poisson ratio, and the Radius of each sphere in contact, respectively. The tangential force F_t depends on the tangential overlap δ_t and the tangential stiffness G^t . The normal damping force F_n^d depends on the coefficient of restitution e , the normal stiffness S_n , the equivalent mass m' , and the normal component of the relative velocity v_n^{rel} . The tangential damping force F_t^d depends on the coefficient of restitution e , the tangential stiffness S_t , the equivalent mass m' , and the tangential component of the relative velocity v_t^{rel} . T_s is the static resistance related to the coefficient of Coulomb static u_s . The rolling resistance T_r depends on the coefficient of the rolling friction u_r , the distance of the

contact point from the center of mass R_i , and the unit angular velocity vector of the object at contact point ω_i .

Input grid and particle data

The data input into the EDEM mainly consisted of grid files and particle data. Grid files are often used to generate a path topography and a particle factory. The particle factory usually appears as a closed container, which determines the position, time, and manner of particle generation. After they are generated by initially modeling using the CAD software, the grid files are imported into the EDEM. In this study, the origin data for the path topography was provided by the pre- and post-digital elevation models (DEMs), which were created from a pre-event topographic map and a post-event aerial image.

According to the field survey results and in view of the cost of the computational time, the particles' radii were random selected with a minimum size of 0.2 m and a maximum of 1.0 m. Before the second landslide, the number of particles was set to be large enough to fill the closed containers of the sliding entrainment and the loading area of the particle factory. The shape of the container was set as a regular hexahedron. After the closed container filled, the container was removed and the dynamic simulation began. Thus the grain distribution pattern was obtained. This procedure is also applicable to the

Table 2 The main micromechanical parameters used in the dynamic particle analysis

Parameter	Value
Particle/path topography density (kg/m ³)	2600/2600
Particle/path topography Poisson's ratio	0.2/0.35
Particle/path topography shear modulus (GPa)	22/6.9
Particle-particle coefficient/particle-path topography static friction	0.5/0.9
Particle-particle coefficient/particle-path topography rolling friction	0.03/0.06
Particle-particle coefficient/particle-path topography restitution	0.5/0.3

formation of existing grains in the landslide–debris avalanche accumulation zone, i.e., the barrier dam formed by the first landslide. Then, the grains in the source area of the second landslide were generated, and the simulation of the movement of the debris avalanche of the second landslide was completed.

Results and discussion

Figures 11 and 12 show the EDEM simulation results of the second Baige rockslide avalanche produced using the Hertz–Mindlin (no slip) contact model. The sliding processes of the rockslide avalanche are shown at different times. The red particles represent the moving landslide materials; the yellow particles represent the first landslide deposit; and the dark particles represent the first debris deposit.

Figures 11a and 12a show the progress of the second landslide at 0 s. The second landslide begins to slide in the source area. The original deposit of the slope is the debris deposit from the first landslide and stays in the relatively flat grooved terrain (range B–C). The debris flow deposit from the first landslide is in the channel of the Jinsha River (range D–E).

Figures 11b and 12b show the progress of the second landslide at 10 s. The landslide mass has already disintegrated, and it is transformed into a rapidly moving debris avalanche, which has a frontal velocity of 17 m/s and is gradually loaded onto the first slide deposit. At this point, the first slide deposit remains stationary as a whole.

Figures 11c and 12c show the progress of the second landslide at 20 s. Due to the dynamic impact and loading of the upper debris avalanche, the first slide deposit is pushed, causing the volume and velocity of the debris avalanche to increase rapidly. The frontal velocity of the debris avalanche reaches 48 m/s.

Figures 11d and 12d show the progress of the second landslide at 30 s. Due to the terrain relief effect, the front slope becomes steeper, the peak velocity of the debris avalanche reaches 62 m/s, and the front of the debris avalanche overlaps the first debris deposit. The large energy entrains the surface material of the first debris deposit, developing into a natural ramp from which grains may leap.

Figures 11e and 12e show the progress of the second landslide at 40 s. As the terrain at the leading edge gradually rises, the debris avalanche assumes a climbing attitude. In addition, the magnitude of the velocity of the incoming grains is preserved after collision. The energy of the debris avalanche

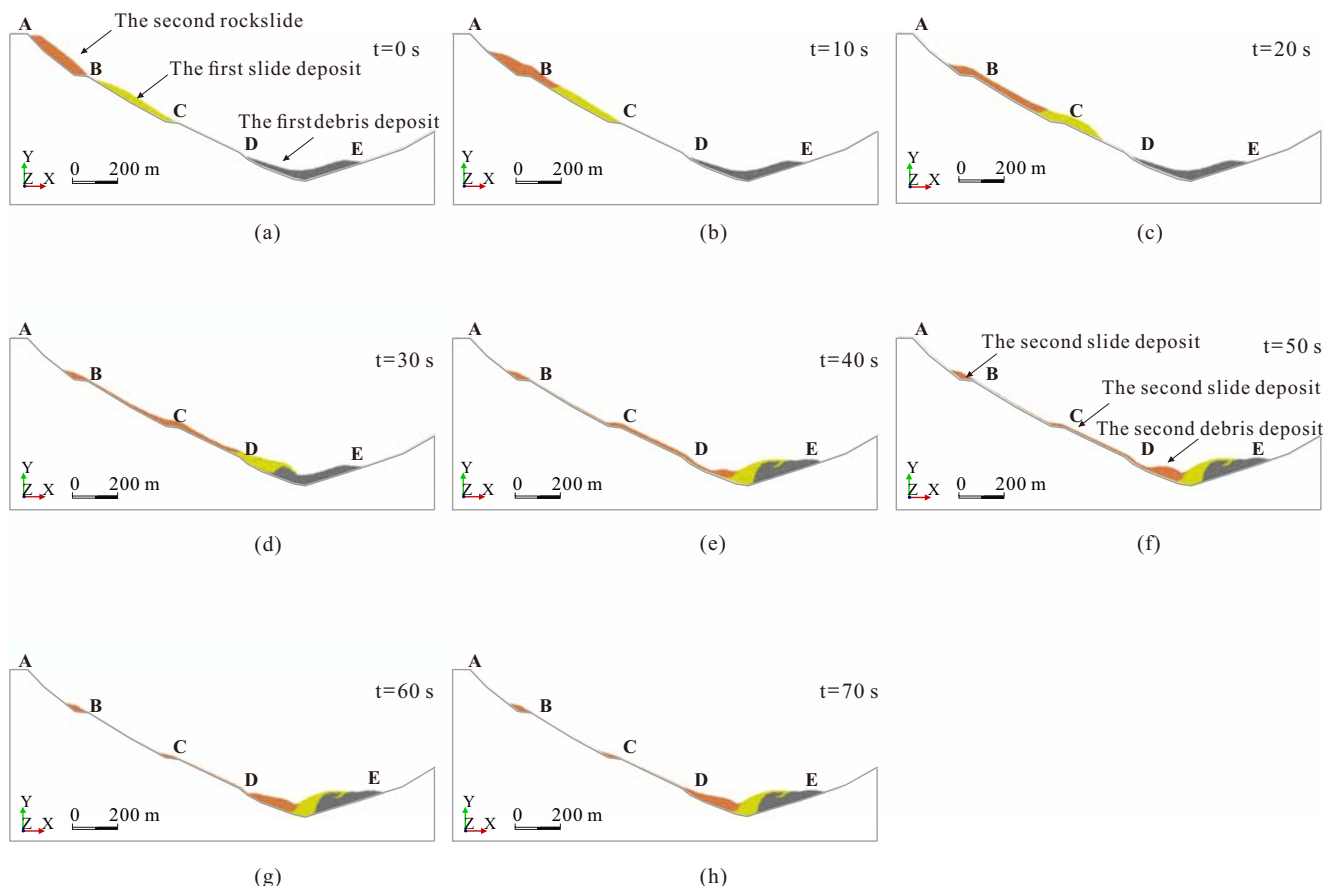


Fig. 11 EDEM simulation results for the second rockslide–debris

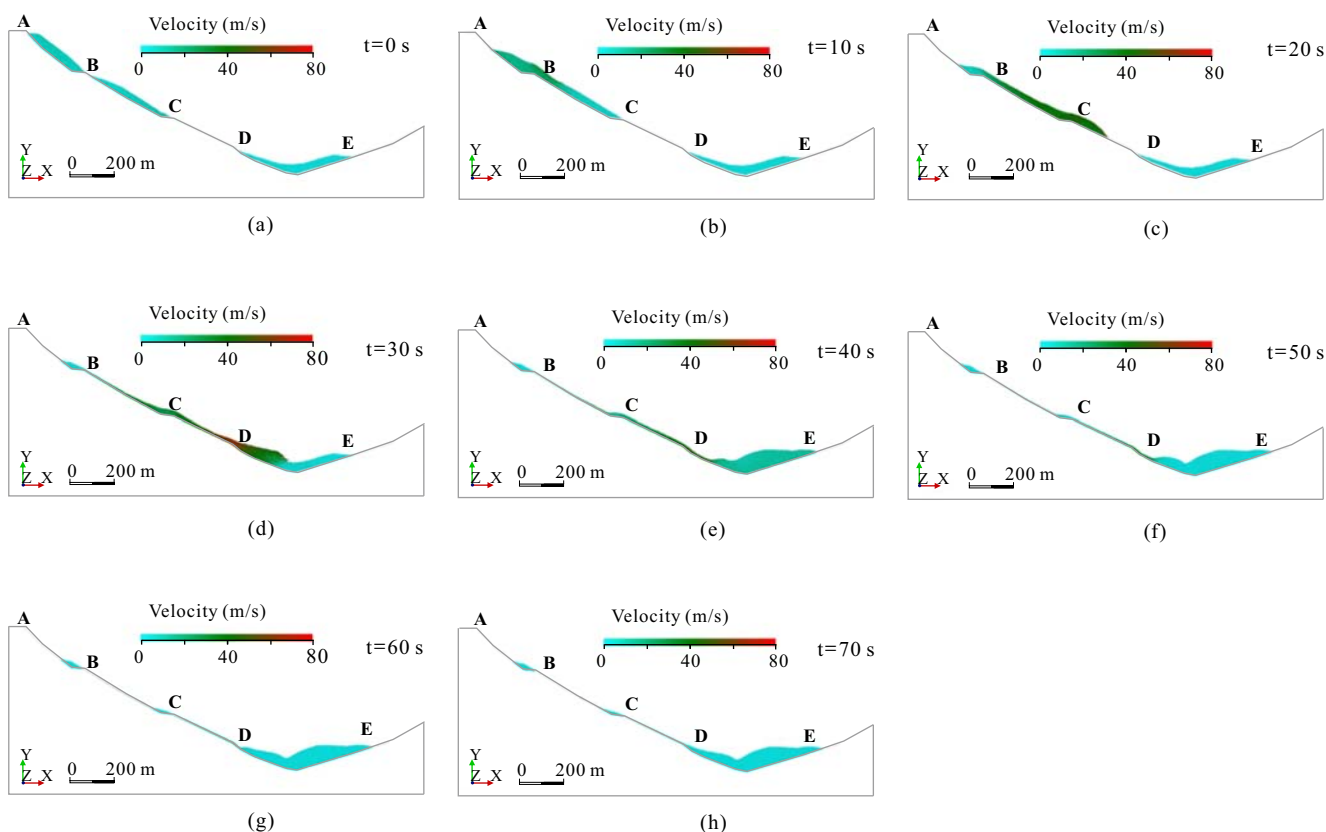


Fig. 12 Velocity evolution results of the second rockslide–debris flow

dissipates gradually, and the peak velocity rapidly drops below 20 m/s.

Figures 11f and 12f show the progress of the second landslide at 50 s. The debris avalanche is basically stationary except some particles with a large velocity of about 40 m/s at the rear part. At this time, the landslide material is mainly deposited in the channel of the Jinsha River, increasing the average height of the dam in the channel by more than 50 m.

Figures 11g and 12g show the progress of the second landslide at 60 s. The debris avalanche is basically stationary except some particles with a velocity of about 20 m/s at the rear part.

Figures 11h and 12h show the progress of the second landslide at 70 s. The debris avalanche is completely stationary. There are still some particles left on the benches of Point B and Point C.

The above numerical simulation fully shows the second sliding process due to accumulated loading effects caused by the impact. It can be also thought as a typical dynamic erosion mode (Fig. 13), quite different from other modes, for instance, the intact rockslide impact and shovel scrap the substrate materials strongly; fragmented landslide impact and plough the substrate materials; flow-like landslide erode the substrate materials gradually (McDougall and Hungr 2005; Pirulli and Pastor 2012). This overloading mode is mainly caused by

the gravity of the upper landslide. In the meantime, there is always a short distance between the upper landslide and the lower deposit. In addition to this landslide, the Xinmo landslide in Maoxian county, Sichuan Province also belongs to this type (Yin et al. 2017). The Fast Lagrangian Analysis of Continua (FLAC) and the slope-stability analysis module of Geo-Studio were once combined to explain the loading effect. However, this combined method cannot completely simulate the whole process of accumulated loading effects caused by the impact (Wang et al. 2019b).

Besides, in order to compare the runout simulation results due to accumulated loading effects, the sled model (Scheidegger 1973) and rheological model (Hungr 1995) are also introduced to establish the relationship between the sliding distance and the maximum velocity of the second Baige landslide (Fig. 14).

The formula of the sled theory can be used easily to estimate the sliding velocity of different location as follows:

$$V = \sqrt{2g(H-f \times L)} \quad (2)$$

where g is the gravitational acceleration; H is the height difference from the starting point to the estimating point; L is the horizontal distance from the starting point to the estimating point; f is the tangent of effective friction angle, which is the

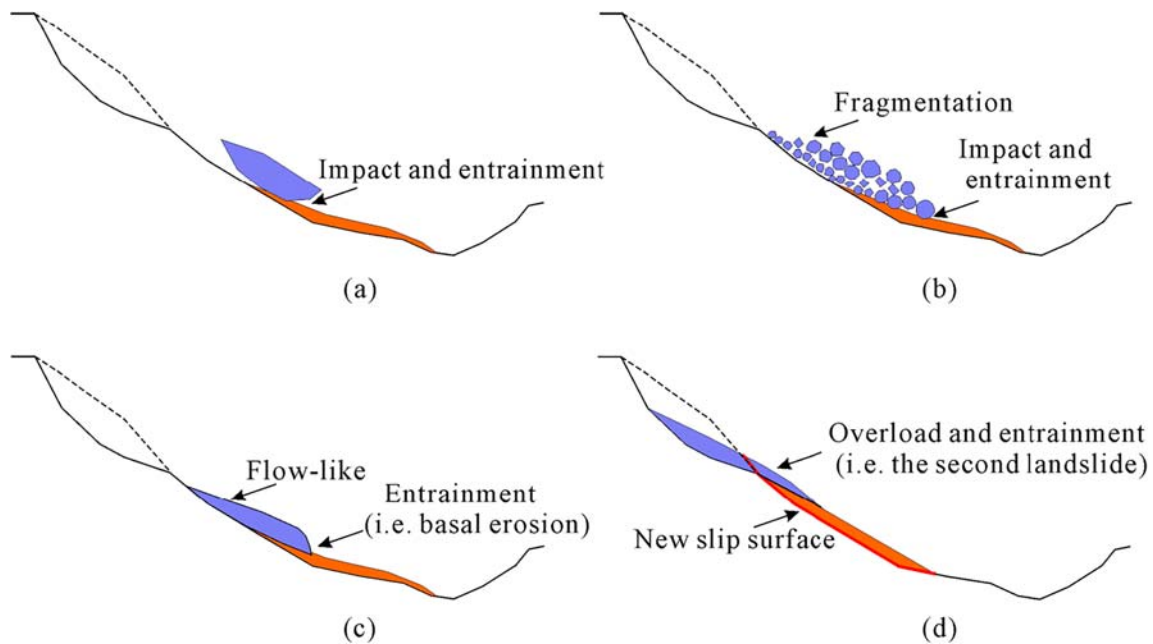


Fig. 13 Four main kinds of dynamic erosion modes due to impacting force. (a) Intact rockslide impact and shovel scrap the substrate materials strongly; (b) fragmented landslide impact and plough the substrate

materials; (c) flow-like landslide erode the substrate materials gradually; (d) secondary sliding due to accumulated loading effects caused by the impact

angle of a line from the avalanche starting point to the most distant end of the debris from the longest running avalanche. From the geometric relationship in Fig. 6, the apparent frictional angle of the landslide and the debris avalanche is approximately 22°.

DAN-W numerical runout software, a rheological model-based program, was also selected to simulate the kinematic motion of the second Baige landslide. The rheological models of friction criterion (F) and the Voellmy criterion (V) had been successfully used to simulate the dynamic process of sliding, shoveling, and accumulation of the Sanxicun landslide (Yin

et al. 2016). The related equations can be found in the paper of Xing et al. (2014). Based on a trial-and-error method and investigation results, the rheology parameters of the F-V model can be determined (Table 3).

In Fig. 14, the debris avalanche formed by the second landslide has a continuously increasing peak velocity in the entrainment and loading zone, promoting a rapid and simultaneous increase in the velocity of the first slide deposit. In addition, due to factors such as the steepening of the terrain, the velocity reaches its peak value of 62 m/s in the accumulation area. Then, the velocity of the debris avalanche decreases rapidly due to the

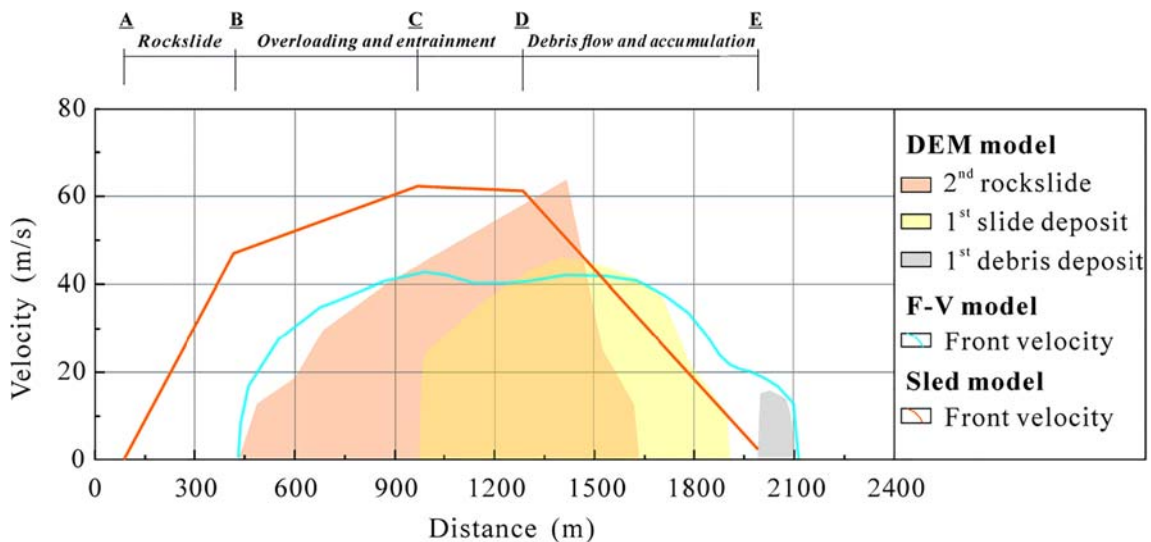


Fig. 14 Comparison of the plots of velocity versus path distance for the second rockslide, the first slide deposit, and the first debris deposit

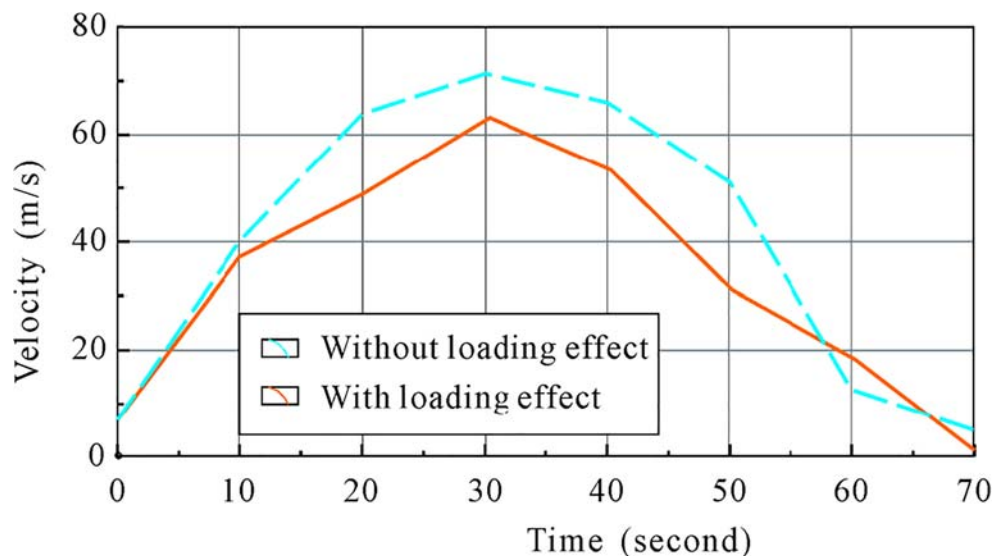
Table 3 Back-calculated values of rheology parameters

Zone	Rheology	φ (°)	f	ξ	Max. erosion depth (m)
Source area	Frictional	10.5	/	/	0
Entrainment area	Voellmy	/	0.2	200	20
Accumulation area	Voellmy	/	0.2	200	0

terrain climbing effect and the energy dissipation caused by the entrainment of the first debris deposit in the channel of the Jinsha River. Compared with the sled model and rheological model, the velocity variation trend versus path distance calculated by DEM model is basically consistent with that of Friction criterion (F) and Voellmy criterion (V) rheological model, both of which is basically smaller than that calculated by sled model. However, the front velocity of the 2nd landslide simulated by DEM can reach a higher peak value, or even exceed the maximum calculation value of sled model. It can be seen that, the peak value of velocity is probably underestimated when the rheological model is used in the overloading and entrainment area, but overestimated in the accumulation area.

In addition, in order to further illustrate that the peak value of the landslide velocity is partly affected by the momentum and energy transfer between the 2nd Baige landslide and the lower accumulation body, the EDEM model of the only upper second landslide is built to compare with the present model, the former of which corresponds to non-considering the accumulated loading effect and the latter is vice versa (Fig. 15).

In Fig. 15, we further compare the maximum velocity versus time for considering or non-considering the accumulated loading effect, and find that if it is not considered, after around 10 s, the peak value of velocity is even larger, which can reach the maximum value of 70 m/s, showing that part of the energy of 2nd landslide is transferred to the lower deposit.

Fig. 15 Comparison of maximum velocity versus time for considering or non-considering the accumulated loading effects

Conclusions

On November 3, 2018, approximately 24 days after the first large-scale landslide, the second Baige rockslide avalanche occurred on the western bank of the Jinsha River. In this study, we introduce the possible failure mechanisms and runout behavior of the landslide based on field investigations and discrete element model simulations. Based on this analysis, we draw the following conclusions.

(a) Two landslides occurred in Baige within a 24-day period and both landslides blocked the river. Therefore, it is necessary to monitor instances of increased deformation and abnormal phenomena in order to predict and evaluate possible blockage of, and damage to, the discharge channel of the barrier dam caused by a third landslide. The possibility of the continuous collapse and slide of the W_block is of particular concern.

(b) In order to enable the early identification of geological disasters, dynamic methods should be used to enhance studies of the disaster mode of the movement process, especially movement modes similar to that of the second Baige landslide. That is, the second sliding event in the source area formed a dynamic impact and trailing-edge loading on the residual rock mass in the central part of the first landslide, rather than merely entraining the lower part of the rock mass to form a rapid long-runout landslide.

(c) In addition, in order to further verify the effectiveness of the DEM model in the simulation of the accumulated loading effects caused by the impact, we select two more models, i.e., sled model and F-V combined rheological model for comparison. The results by the DEM and F-V combined rheological models are both closer to each other, except that the 2nd landslide could reach the highest peak value of about 62 m/s. It is still a bit less than the peak value of velocity of non-considering the accumulated loading effect, which shows that part of the energy of 2nd landslide is transferred to the lower deposit of considering the accumulated loading effect.

(d) Compared with the DEM model, the peak value of velocity is probably underestimated when the rheological model is used in the overloading and entrainment area, but overestimated in the accumulation area. Of course, similar comparisons will be made in the future to better illustrate the applicability of various models.

Acknowledgments We are grateful to Geological Engineering Investigation Institute, MeiShan for supplying some field survey data. We are also grateful to Engineer Yiqiu Deng and Engineer Ming Gong from Hi-key Technology for their help in EDEM software operation. In addition, we are also grateful to the Editor in Chief of Bulletin of Engineering Geology and the Environment, Louis N.Y. Wong, for reconsidering the revised manuscript. Finally, the authors would like to thank the reviewers of this manuscript for their good suggestions and useful comments.

Funding information The study was financially supported by the National Key R&D Program of China (Grant No. 2018YFC1505404), National Natural Science Foundation of China (No. 41731287), and Geological Disaster Detailed Investigation Project of China Geological Survey (Grant No. DD20190637).

References

- Cagnoli B, Piersanti A (2017) Combined effects of grain size, flow volume and channel width on geophysical flow mobility: three-dimensional discrete element modeling of dry and dense flows of angular rock fragments. *Solid Earth* 8:177–188
- Chen DN, Sarumi M, Al-Hassani STS (1998) Computational mean particle erosion model. *Wear* 214:64–73
- Cundall PA, Strack O (1979) A discrete numerical model for granular assemblies. *Geotechnique* 29:47–65
- Davies T, McSaveney MJ (1999) Runout of dry granular avalanches. *Can Geotech J* 36:313–320
- Deng JH, Gao YJ, Yu ZQ, Xie HP (2019) Analysis on the formation mechanism and process of baige Landslides damming the upper reach of Jinsha River, China. *Adv Eng Sci* 51(1):9–16 (in Chinese)
- EDEM (2018) Website, <https://www.edemsimulation.com/>
- Fan XM, Xu Q, Scaringi G, Dai LX, Li, Dong XJ, Zhu X, Pei XJ, Dai KR, Havenith HB (2018) Failure mechanism and kinematics of the deadly June 24th 2017 Xinmo landslide, Maoxian, Sichuan, China. *Landslides* 14(9):2129–2146
- Fan XM, Xu Q, Alonso-Rodriguez A, Subramanian S, Li WL, Zheng G, Dong XJ, Huang RQ (2019) Successive landsliding and damming of the Jinsha River in eastern Tibet, China: prime investigation, early warning, and emergency response. *Landslides* 16(5):1003–1020
- Feng ZY, Lo CM, Lin QF (2017) The characteristics of the seismic signals induced by landslides using a coupling of discrete element and finite difference methods. *Landslides* 14(2):661–674
- Hungr O (1995) A model for the run out analysis of rapid flow slides, debris flows, and avalanches. *Can Geotech J* 32:610–623
- Hungr O, McDougall S (2009) Two numerical models for rockslide dynamic analysis. *Comput Geosci* 35:978–992
- Kang C, Chan D (2018) Numerical simulation of 2D granular flow entrainment using DEM. *Granul Matter* 20(13):1–17
- McDougall S, Hungr O (2005) Dynamic modelling of entrainment in rapid landslides. *Can Geotech J* 42(5):1437–1448
- McSaveney MJ, Davies TR (2007) Rockslides and their motion, Chapter 8. In: Sassa K, Fukuoka H, Wang F, Wang G (eds) *Progress in landslide science*. Springer, Heidelberg, pp 113–133
- Ouyang CJ, An HC, Zhou S, Wang ZW, Su PC, Wang DP, Cheng DX, She JX (2019) Insights from the failure and dynamic characteristics of two sequential landslides at Baige village along the Jinsha River, China. *Landslides* 16(7):1397–1414
- Pirulli M, Pastor M (2012) Numerical study on the entrainment of bed material into rapid landslides. *Geotechnique* 62(11):959–972
- Sassa K, Nagai O, Solidum R et al (2010) An integrated model simulating the initiation and motion of earthquake and rain induced rapid landslides and its application to the 2006 Leyte landslide. *Landslides* 7(3):219–236
- Sassa K, He B, Dang K, Nagai O, Takara K (2014) Plenary: progress in landslide dynamics. In: Sassa K, Canuti P, Yin YP (eds) *Landslide science for a safer geoenvironment*. Springer International Publishing, Switzerland, pp 37–67
- Scheidegger AE (1973) On the prediction of the reach and velocity of catastrophic landslides. *Rock Mech Rock Eng* 5(4):231–236
- Tsuji Y, Tanaka T, Ishida T (1992) Lagrangian numerical simulation of plug flow of cohesionless particles in a horizontal pipe. *Powder Technol* 71:239–250
- Wang LC, Wen MS, Feng Z, Sun WF, Wei YJ, Li JF, Wang WP (2019a) Researches on the Baige landslide at Jinshajiang River, Tibet, China. *The Chinese Journal of Geological Hazard and Control* 30(1):1–9 (in Chinese)
- Wang WP, Yin YP, Yang LW et al (2019b) Investigation and dynamic analysis of the catastrophic rockslide avalanche at Xinmo, Maoxian, after the Wenchuan Ms 8.0 earthquake. *Bull Eng Geol Environ*. <https://doi.org/10.1007/s10064-019-01557-4>
- Xing AG, Wang GH, Li B et al (2014) Long-runout mechanism and landsliding behaviour of large catastrophic landslide triggered by heavy rainfall in Guanling, Guizhou, China. *Can Geotech J* 52(7):971–981
- Xu Q, Zheng G, Li WL, He CY, Dong XJ, Guo C, Feng WK (2018) Study on successive landslide damming events of Jinsha River in Baige Village on October 11 and November 3, 2018. *J Eng Geol* 26(6):1534–1551 (in Chinese)
- Yin YP, Cheng YL, Liang JT, Wang WP (2016) Heavy-rainfall-induced catastrophic rockslide debris flow at Sanxicun, Dujiangyan, after the Wenchuan Ms 8.0 earthquake. *Landslides* 13(1):9–23
- Yin YP, Wang WP, Zhang N, Yan JK, Wei YJ, Yang LW (2017) Long runout geological disaster initiated by the ridge-top rockslide in a strong earthquake area: A case study of the Xinmo landslide in Maoxian County, Sichuan Province. *Geol China* 44(5):827–841 (in Chinese)
- Zhang M, McSaveney MJ (2017) Rock avalanche deposits store quantitative evidence on internal shear during runout. *Geophys Res Lett* 44(17):8814–8821